frontiers | Frontiers in Mechanical Engineering

TYPE Original Research
PUBLISHED 24 March 2025
DOI 10.3389/fmech.2025.1478081

OPEN ACCESS

EDITED BY
Hailin Li,
West Virginia University, United States

REVIEWED BY
Bart Somers,
Eindhoven University of Technology, Netherlands
Duygu Ipci,
Gazi University, Türkiye

*CORRESPONDENCE
Rafael Menaca,
rafael.menaca@kaust.edu.sa

RECEIVED 09 August 2024
ACCEPTED 04 March 2025
PUBLISHED 24 March 2025

CITATION
Menaca R, Silva M, Uddeen K, Almatrafi F, Tang Q, Turner JWG and Im HG (2025) Optical multi-spark ammonia combustion engine: numerical analysis and validation.
Front. Mech. Eng. 11:1478081.
doi: 10.3389/fmech.2025.1478081

Optical multi-spark ammonia combustion engine: numerical analysis and validation

Rafael Menaca[1]*, Mickael Silva[2], Kalim Uddeen[1], Fahad Almatrafi[1], Qinglong Tang[3], James W. G. Turner[1] and Hong G. Im[1]

[1]Clean Energy Research Platform (CERP), King Abdullah University of Science and Technology, Thuwal, Saudi Arabia, [2]Aramco Americas: Aramco Research Center, Detroit, MI, United States, [3]State Key Laboratory of Engines, Tianjin University, Tianjin, China

Ammonia (NH_3) stands out as a promising candidate for fueling internal combustion engines, owing to its high hydrogen content and well-established production and transport infrastructure. Nevertheless, its inherently low flame speed and reactivity pose a significant challenge to achieving rapid and complete combustion. One potential solution is the use of multi-spark ignition, wherein multiple spark plugs distribute ignition sites throughout the combustion chamber, thereby accelerating flame propagation across the entire charge. In this study, a three-dimensional 3D-CFD model of multi-spark, spark-ignited NH_3 internal combustion engine is developed and validated using optical engine experiments. The optical data provide critical insights into early flame kernel development, guiding refinements to two combustion submodels (SAGE and G-equation). Results underscore the importance of sufficiently refined mesh resolution—particularly near the spark plugs—and the incorporation of detailed spark plug geometries to accurately capture the early stages of ignition in low-reactivity fuels such as NH_3. Overall, the close qualitative agreement between measured flame luminosity and simulated flame evolution demonstrates the robustness of the proposed CFD framework.

KEYWORDS

ammonia, Ignition strategies, spark ignition, optical engine, ammonia combustion modeling

1 Introduction

Meeting world energy demands relies primarily on the utilization of hydrocarbon fuels. The transport sector represents about 20% of total energy consumption, with road mobility accounting for 72% of this fraction Bilgen (2014). In the U.S., the transportation sector is the leading emitter of greenhouse gases EPA (2024). To achieve future international environmental goals, a mix of technologies has been proposed in recent years to reduce the overall fleet emissions. This can be accomplished either by enhancing engine efficiency or by utilizing alternative fuels with minimal carbon emissions. Ammonia (NH_3) emerges as a promising candidate for direct application in internal combustion (IC) engines as a carbon-free fuel, benefiting from its high hydrogen content. The NH_3 production and transportation industry is well-established, reducing barriers for near-future deployment.

In the spark-ignited (SI) application, due to the high-octane number of NH_3, engines can operate at high compression ratios without abnormal combustion. However, a major challenge of NH_3 combustion in SI engines is its significantly slow flame speed, which limits the operation range. Tornatore et al. (2022) showed that a conventional solution to boost the flame speed is the use of blends with faster-burning fuels, such as hydrogen, thus

enhancing burning rate and extending the operation range. Literature suggests a general consensus in the need of a combustion enhancer for the pure NH_3 SI engine combustion, such as hydrogen or methane, if the engine is required to operate in the entire load range with reduced variability and acceptable indicated efficiencies. Multiple studies have demonstrated that this effect may improve flame speed, combustion stability, while reducing unburned NH_3 emissions as summarized by El-Adawy et al. (2024). In general, power output similar to those of conventional gasoline engines may be achieved via co-optimization of engine design and operation strategies.

Additionally, different techniques for NH_3 combustion in IC engines was outlined by Chiong et al. (2021). They highlight that NH_3 may be dissociated to produce *in situ* hydrogen, reducing the barriers for deployment, such as system modification for multiple injectors and fuel storage systems, with a compatible catalytic converter; the *in situ* cracking of NH_3 can result in the same effect of hydrogen enrichment for reactivity boost. Mercier et al. (2022) reported a reduction in the mixture energy content when cracking the NH_3. Additionally, it was shown that the overall system efficiency is inferior, especially when considering the required energy for dissociating the NH_3, although recent reports, summarized by Tornatore et al. (2022), demonstrate that the endothermic reactions for NH_3 cracking may be assisted by the recovery of the engine exhaust heat.

An alternative approach to increasing the burning rate in NH_3 combustion is the use of multiple spark plugs. Uddeen et al. (2023a); Uddeen et al. (2023b); Uddeen et al. (2023c) have investigated this technique, which enables multiple flame kernels to grow, collapse, and cover the entire combustion chamber quickly and stably, thereby improving efficiency and reducing variability. Their studies found that, compared to a single spark, the multi-spark ignition strategy increases in-cylinder pressure, shortens the combustion duration, and enhances engine stability due to the improved NH_3 fuel combustion rate. Furthermore, the coefficient of variation (COV) was significantly reduced from 19.58% with a single spark to 1.96% with multi-spark operation. Additionally, natural flame luminosity (NFL) imaging evaluation revealed a considerable boost in flame intensity and surface area.

Silva et al. (2023) conducted a computational fluid dynamics (CFD) assessment to determine the optimal engine operating conditions for achieving maximum efficiency with pure NH_3. Their findings highlight the necessity of advancing the spark timing (ST) to maximize combustion efficiency. Moreover, the low reactivity of NH_3 resulted in poor combustion with elevated levels of unburned fuel, a problem further exacerbated at higher engine speeds where increased turbulence did not adequately compensate for the reduced residence time for combustion. The local flow analysis revealed that most of the combustion occurred in the corrugated flamelet regime, and the burning rate was dominated by the laminar flame speed, suggesting the need for fuel blending. Yang et al. (2023) proposed a chemistry model for pure NH_3 combustion, incorporating a decoupled approach for fuel NO_x and thermal NO_x formation. Subsequently, Huang and Liu (2024) expanded this model to investigate the acceleration of combustion via multiple sparks. Their findings showed an increase in the pressure rise rate while keeping it within safe limits. They reported a global enhancement in the burning rate and an improvement in fuel economy. Despite the advancements reported in these studies, discrepancies arise when comparing their results to our findings, particularly regarding flame topology. While the multi-spark technique demonstrated significant benefits, the variations in flame structure highlight the need for further investigation and refinement.

Building on the prior modeling experience, this study attempts to develop an improved computational fluid dynamics (CFD) simulation practices as a means to guide the development of successful NH_3 multi-spark SI engines. First, data from optical engine experiments are employed to validate a numerical model for the SI multi-spark NH_3 engine operation. An in-depth analysis of the multiple flame behavior is presented with comprehensive assessment of required mesh, heat transfer models, ST, and mixture composition. Two typically used combustion models (SAGE and G-Equation) are assessed, showing their feasibility for NH3 engine modeling when appropriately choosing the chemistry set and model constants; the optical engine results are further correlated with the turbulence-chemistry interaction captured in the CFD simulations. The extensive analysis leads to identifying best strategies in CFD engine modeling for predicting the complex NH_3 multi-flame interactions. By offering comprehensive modeling guidance for similar NH_3 engines, this study aims to pave the way for future optimization investigations within the research community.

2 Optical experiments

The experiment was performed on a single-cylinder four-stroke optical research compression-ignition engine (AVL-5402), which was converted into SI engine conditions. An AVL PUMA automation system (V2012) was used to control and monitor the engine conditions. The combustion was initiated by four side spark plugs (ER8EH, NGK), which were equally spaced and installed around the circumference of a specialized metal liner labeled from SP 1 to 4, and another spark plug (C) mounted at the top of the cylinder head. Additionally, an AVL-GU22CK pressure transducer (T) was installed on the top of the cylinder head to record the in-cylinder pressure. A flat-quartz, extended Bowditch piston (Suprasil 2 grade B) was employed, as seen in Figure 1. To capture the flame images from below, a 45^o UV mirror at the bottom side of the combustion chamber was placed. A high-speed Photron SA4 color camera was used to capture NFL images generated by flame propagation from different ignition sites. The camera was triggered at 36,000 frames per second to observe the flame propagation. The engine schematic and details of the engine parameters are presented in Figure 1; Table 1. This study numerically validated the results of the five-spark ignition "SP (1234C)" configuration at a ST of −30 CAD aTDC. Furthermore, the engine was consecutively operated for 200 firing cycles. A detailed description of the experimental setup and operating conditions can be found in Refs. Uddeen et al. (2023a); Uddeen et al. (2023b); Uddeen et al. (2023c).

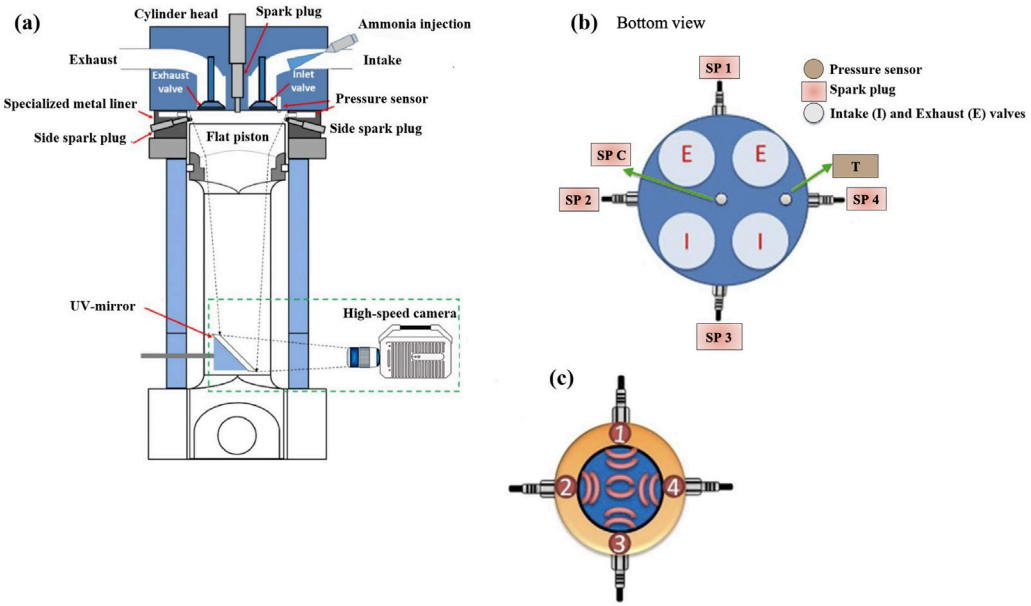

FIGURE 1
a) Schematic of the setup, **(b)** bottom view of the combustion chamber arrangement, highlighting the multiple spark locations, and **(c)** flame front development patterns Uddeen et al. (2023a); Uddeen et al. (2023b); Uddeen et al. (2023c).

TABLE 1 Engine specifications.

Description	Specification
Type	Single-cylinder optical research engine
Swept volume	511 cc
Compression ratio	10.5
Bore	85 mm
Stroke	90 mm
Piston geometry	Flat
Number of valves	Intake (2), Exhaust (2)
Valve type	DOHC
Intake valve	Open 10°CA bTDC
	Close 50°CA aBDC
Exhaust valve	Open 60°bBDC
	Close 0°aTDC

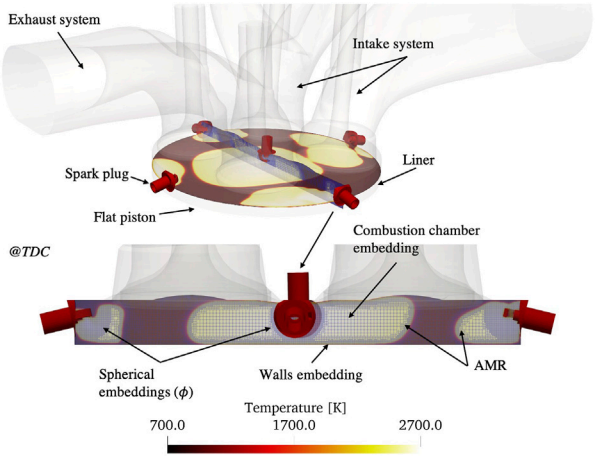

FIGURE 2
Computational domain and mesh characteristics.

3 Computational model

3.1 Numerical configuration

The AVL optical engine was modeled and the numerical simulations were executed by the density-based finite volume CFD solver CONVERGE^{TM} 3.0 utilizing its multi-physics capabilities Richards et al. (2021). The computational domain is illustrated in Figure 2. The Reynolds-averaged Navier-Stokes (RANS) formulation was used with the RNG $\kappa - \epsilon$ closure model Han and Reitz (1995). Pressure-implicit with splitting of operators (PISO) algorithm was employed to couple pressure and velocity dynamics Issa et al. (1986). Wall heat transfer was modeled with the GruMo-UniMORE model developed by Berni et al. (2017). The Redlich-Kwong equation of state was used along with real gas properties and mixture-averaged diffusion coefficients. Turbulent Prandtl and Schmidt numbers were set as 0.9 and 0.78, respectively. The multi-zone well-stirred reactor (MZ-WSR), referred to as SAGE, combustion model was selected as a baseline combustion submodel, with the kinetic mechanism by Zhang et al. (2021). Furthermore, G-equation combustion model is assessed. The

TABLE 2 Mesh features in the mesh sensitivity analysis.

Refinement technique \Case	Baseline	Mesh 1	Mesh 2	Mesh 3	Mesh 4
Spark spherical embedding*	$\phi = 5mm$ Level 2	$\phi = 5mm$ Level 4	$\phi = 10mm$ Level 4	$\phi = 10mm$ Level 4	$\phi = 10mm$ Level 4
Combustion chamber region embedding	No	No	No	Level 2	Level 2
Adaptive mesh refinement Based on velocity and temperature	No	No	No	Level 4	Level 4
Spark plug geometry	No	No	No	No	Five spark plugs

* ϕ: spherical embedding diameter.

initial field variables were mapped from a prior simulation to replicate the effects of field initialization. The simulations began at −175 CAD and continued until 900 CAD, thereby covering a full cycle. Variable time-step algorithm was implemented with the minimum time step governed by the critical Courant-Friedrichs-Lewy number.

Boundary conditions were imposed based on the experimental measurements Uddeen et al. (2023a); Uddeen et al. (2023b); Uddeen et al. (2023c). The mixture composition was stoichiometric and assumed as a perfectly mixed inflow boundary condition. Constant Dirichlet pressure inlet and outlet boundary conditions were set, simplifying the exchange gases process, yet capturing the correct delivered mass per cycle. Piston, liner and head walls temperatures were kept at 450 K, while the intake and exhaust systems temperatures were maintained at 333 K and 500 K, respectively. To model ignition, a spherical energy source was placed at each spark plug electrode gap. The ST was set to −30 CAD. For G-equation, ignition was achieved using passive source modeling with a $G = 0$ surface initialized at the spark location as a spherical surface of 0.5 mm. Alternatively, the multi-zone well-stirred reactor model used a high- and low-energy source to capture ignition, depositing 0.04 J and 0.02 J in a spherical region of 0.5 mm radius over 0.5 CAD and 10 CAD, respectively. The five-spark combustion configuration was selected for evaluation because it operates at a low COV, making the experimental data a reliable baseline for modeling. A base mesh size of 2.5 mm was employed throughout the entire domain. Furthermore, adaptive mesh refinement (AMR) was applied in regions with strong gradients in temperature and velocity, and embedded mesh refinement was used to capture near-wall flow characteristics. Spherical embeddings were implemented around the spark plug regions. Mesh features are shown in Figure 2, and details are provided in Table 2 for the five different configurations that were evaluated.

3.2 Validation stage and simulation strategy

The first step in the calibration of the engine model was related to the proper representation of the compression and expansion of the in-cylinder gases. Optical engines experience a significant level of leakage due to hardware modifications and the setup configuration. Therefore, to assure accurate reproduction of the pressure history, a proper crevice model is crucial. Following the studies by Irimescu et al. (2013); Irimescu et al. (2018); De Renzis et al. (2021), 7.5% of the total inducted mass per cycle was allowed to leak to the crankcase. The model was further calibrated while maintaining

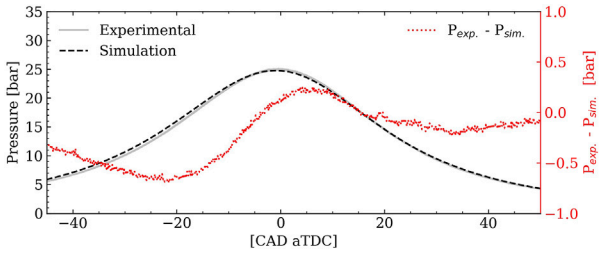

FIGURE 3
Motoring pressure evolution comparison between experiments and numerical results.

the squish height as in the engine, leading to a geometrical compression ratio of 12. The results are presented in Figure 3, revealing close agreement with the experimental data, particularly during the expansion stroke. This level of accuracy is especially noteworthy given the optical configuration of the engine under investigation.

Subsequently, combustion cases are calibrated, starting from mesh sensitivity; different mesh strategies were tested and as summarized in Table 2. The baseline case setup is established based on literature Yang et al. (2023), whereas the additional mesh features were considered to improve the description of the initial kernel growth with the refinement of the mesh in the spark plug region. Additionally, a cylindrical embedding of the combustion chamber was explored in meshes three and four to observe the keys aspects of the main chamber turbulence dissipation, along with the AMR to refine the flame zones. Finally, the geometry of all the spark plugs was introduced in Mesh four and its effects on the combustion behavior will be explained in detail below.

4 Assessment of numerical parameters

4.1 Mesh sensitivity analysis

Figure 4a presents the pressure and apparent heat release rate (AHRR) evolutions for the different evaluated cases, with 100 experimental combustion cycles shown in gray for reference. At first glance, the Baseline, Mesh 1, and Mesh two simulations underpredict the pressure rise despite accurately capturing the ignition delay, indicating a slower heat release rate compared to the experiments. This discrepancy can be attributed to the coarse

mesh resolution in the spark plug region and insufficient refinement during the early stages of combustion. In particular, coarse meshes promote a rapid energy dissipation, which reduces the reactivity of the cell-based ignition in the SAGE combustion model.

Additional evidence appears in Figure 4b, which shows how the temperature in the SPC vicinity rapidly decays for the coarse meshes. In the Baseline mesh, the peak temperature is even lower due to this rapid energy dissipation. A second temperature peak occurs once combustion initiates; notably, this peak appears earlier for Mesh three and takes longer in the coarser meshes, indicating a slower heat release process.

In contrast, Mesh three overpredicts the heat release rate and the peak pressure reaches higher values compared to experiments. Although the mesh in the spark plug surroundings is refined, as well as the combustion chamber, the early flame development is shorter and a rapid rise of the in-cylinder pressure is substantial. To understand how the local flow field and early flame development are affected by the presence of spark plugs geometry (J-gap type), their geometrical details are included in Mesh 4. Remarkably, the prediction is much improved, suggesting the importance of capturing the near-spark flow field during the early combustion development. To obtain additional insights about the importance of the detailed geometry, additional test simulations were done with the spark plugs rotated (results not shown in the document), but marginal changes were observed in the numerical results. It is thus concluded that the most important aspect is the local flow field near the wall.

These findings suggest that typical engine CFD meshing practices for hydrocarbon fuels may not be fully applicable to NH_3-fueled engines, primarily due to NH_3's lower reactivity and narrower flammability range. Under coarse mesh resolutions, numerical dissipation can quickly dilute the ignition kernel and reduce reactivity, making it more difficult to accurately capture the onset and early stages of NH_3 combustion.

4.2 Effect of heat transfer model

Different heat transfer models may be selected for the law-of-the-wall temperature boundary condition treatments available in CONVERGE, such as GruMo-UniMORE by Berni et al. (2017), Amsden, 1997, and Han and Reitz (1997). A proper heat transfer description is necessary to correctly describe the flow physics in the combustion chamber, especially at the end of the compression stroke and during combustion period when the walls are experiencing higher heat transfer rates. As the viscous sublayer is not resolved, it is necessary to model the temperature profile near the wall. In addition to the heat transfer equation, the transition of the logarithmic layer, y^+, is also important. In general, the GruMo-UniMORE model is recommended for highly-charged/highly-downsized spark-ignited engines and account for different transient elements during the power cycle; Han and Reitz incorporates compressible effects and offers a transient description of the heat transfer processes; O'Rourke and Amsden rely on the quasi-steady assumption, where the heat transfer process has reached a local equilibrium.

Figure 5 shows that the implementation of the three different models lead to a similar behavior in the pressure and AHRR evolution, with the O'Rourke model predicting a slightly higher peak pressure and AHRR. This suggests that the heat losses are minimal when using this model. On the other hand, the AHRR peak in GruMO-UniMORE and Han and Reitz is similar, with the latter predicting a longer combustion duration. In addition, the pressure peak is lower for the Han and Reitz results, indicating higher heat transfer losses, observed as well in the lower pressure captured towards the end of the compression stroke. Considering the small variations, for this specific engine configuration running with NH_3 as fuel, any of the three heat transfer

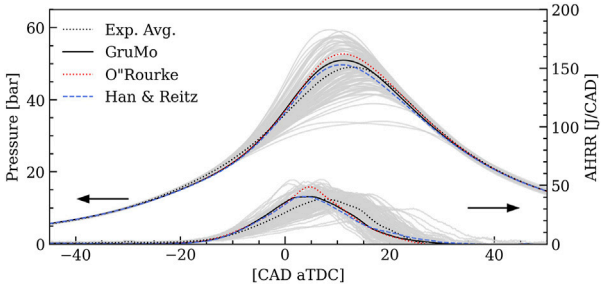

FIGURE 5
Pressure and AHRR traces for the different evaluated heat transfer models.

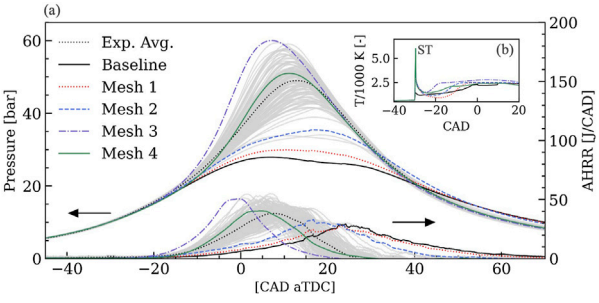

FIGURE 4
(a) Pressure evolution and AHRR, and **(b)** volume-averaged temperature in the SPC region during the energy deposition period, for the various cases evaluated in the mesh sensitivity analysis.

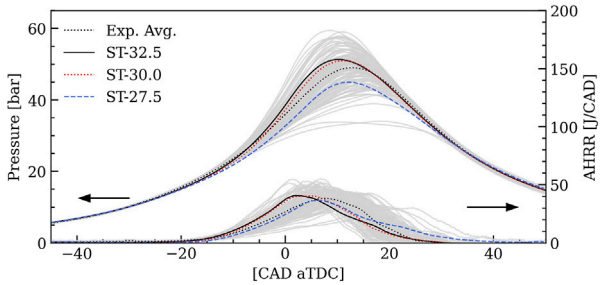

FIGURE 6
Pressure and AHRR traces for the different evaluated STs.

models are found to be adequate in predicting the engine combustion behavior.

4.3 Effect of spark timing

The reference ST was set at −30 CAD aTDC. Given the lack of data in optical NH_3 engines, however, the uncertainties in arc breakdown timing were assessed by varying the ST by ± 2.5 CAD, as shown in Figure 6. Although the AHRR rise begins at a similar time for earlier STs, the retarded ST exhibits a significant ignition delay. Furthermore, the three cases demonstrate distinct pressure evolutions. A monotonic reduction in the pressure peak and an increased ignition delay are observed with retarded STs. These results indicate that while the HRR for earlier STs remains similar, the retarded case shows a significantly lower peak. Due to the slow flame speed of NH_3, delaying the ST results in a substantial reduction in both pressure peak and AHRR, along with a further delayed ignition. However, more data is needed to draw a conclusive understanding of the sensitivity to ST.

5 Combustion modeling and flame behavior

5.1 Natural flame luminosity

To further demonstrate the fidelity of the model, the instantaneous flame development and topology is analyzed in Figure 7. In the first row (a) optical experiments are presented, whereas the second row (b) shows the computational volumetric rendering of the temperature field. Upon initial inspection, the CFD results demonstrate a qualitatively accurate prediction of flame development from the five different spark locations. However, the numerically predicted flame growth appears slightly faster than in the experiments, which may relate to the higher AHRR observed in Mesh 4 (see Figure 4). Furthermore, it should be noted that the experimental optical setup does not capture the entire outer region of the combustion chamber, and the single-shot image from the experiment may differ from the ensemble-averaged RANS solution. In the initial stages of combustion at −10 CAD, the flame surface areas are small, and then grow towards top dead center (TDC), increasing the pressure and temperature of the combustion chamber. At 10 CAD, the different flame fronts have merged towards the late combustion, consuming nearly the entire unburned premixed charge. As reported in previous studies by Huang and Liu (2024), the multi-spark methodology speeds up the overall charge consumption due to the simultaneous creation of multiple flame fronts. One important observation is the flame resultant from the central spark (SPC) growing with a faster rate. Furthermore, it is observed that the topology for the different flames differ among them, as further discussed later.

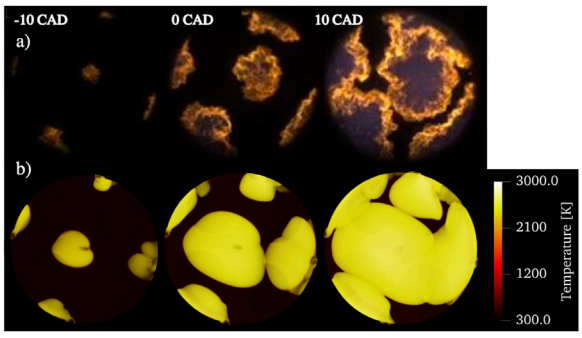

FIGURE 7
Flame development viewed from the bottom captured by **(a)** natural flame luminosity experiments and **(b)** numerical results with Mesh 4 model. Volumetric post-processing for the temperature field.

5.2 Flame dynamics

The volumetric-averaged turbulent kinetic energy (TKE) at each spark location is presented in Figure 8. There are two important peaks during the cycle. The first one corresponds to the intake valve opening event, promoting the increase in the TKE as a consequence of the entering turbulent inflow mixture charging the main chamber. The second peak occurs at the ST, where the sudden rise in the pressure and the expansion of the flames disturb the local flow field. It is seen that TKE is higher at SPC before the start of ignition, which promotes the central flame to grow faster. Additionally, higher fluctuations are observed in this region. There is irregular behaviors in the different regions during the intake stroke. However, the level of turbulence decays once the intake valves are closed. Towards the compression stroke, the fluctuations in the flow field remain at similar low values.

It is evident that each flame front behaves distinctly as a consequence the different local flow field conditions at ST and afterwards; this implies the need for appropriate mesh selections at different regions to capture the detailed turbulent flow characteristics in addition to the spark geometry. Furthermore, due to the turbulent flows and the swirl-type engine, the in-cylinder fluid dynamics varies spatially, translating in a complex flame-flame interaction. The present results show significant differences from those obtained by Huang and Liu (2024), where a simplified initial setup resulted in multiple flame fronts propagating in comparable shapes and sizes. The present study

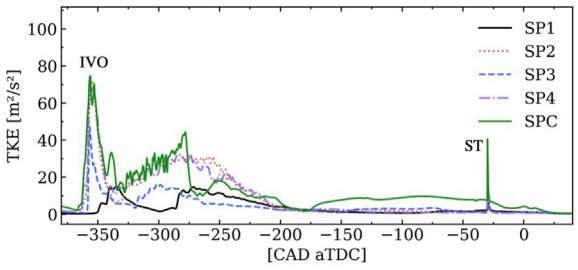

FIGURE 8
Volume-averaged TKE evolution at the five different spark plug regions.

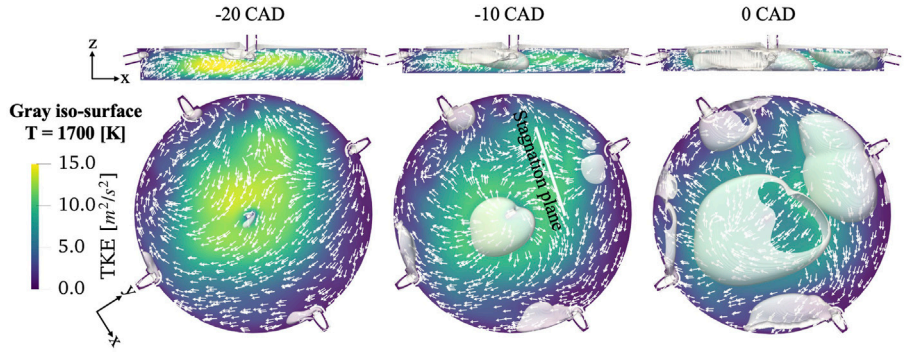

FIGURE 9
Vector field, TKE profile and iso-surface for T = 1700 K, at different timings in the combustion chamber. Top: xz-plane view; Bottom: rotated xy-plane at z = −3 mm.

suggests that capturing local variations in the flow and flame behavior may lead to a significant difference in the prediction of the overall engine combustion characteristics.

More details of the flow field are shown in Figure 9 along with the TKE map. The higher TKE found in the center of the combustion chamber is found to be caused by the swirl motion. The rotational motion promotes an increase in the pressure close to the walls, where the velocity is zero due to the non-slip condition; the boundary layers of the piston and head induce the flow to move inwards to the center of the combustion chamber. As a consequence of the different streams collapsing, velocity fluctuations are concentrated in that region. The iso-surface for T = 1700 K represents the flames in Figure 9. Due to the growth of the multiple flames and the heat release during combustion, the gas expansions at different locations affects the flow patterns, where multiple locus of flow stagnation are observed as a result of the flames propagating onto the fresh charge.

5.3 Turbulence-chemistry interaction

Turbulence varies significantly both spatially and temporally throughout the cycle. These variations have a crucial influence on flame dynamics and need to be properly captured in the model. The SAGE combustion model treats each computational cell as a homogeneous (well-stirred) reactor. Accordingly, within the RANS framework, turbulence-chemistry interactions (TCI) are effectively neglected, as local reaction rates are computed solely from the mean flow field and temperature without accounting for sub-grid fluctuations Mohan and Haworth (2015). To properly account for TCI in the context of flame propagation, the G-Equation combustion model is being employed, where a transport equation for the scalar field variable G is solved and the iso-scalar surface $G(\mathbf{x},t) = G_0$ represents the flame surface at each instantaneous solution field, separating the burned and unburned gases. The proposed transport equation per Peters (2001) is written as:

$$\frac{\partial \rho \tilde{G}}{\partial t} + \frac{\partial \left(\rho \tilde{u}_i \tilde{G}\right)}{\partial x_i} = \rho_u S_t \left|\frac{\partial \tilde{G}}{\partial x_i}\right| - \rho D_t' \kappa \left|\frac{\partial \tilde{G}}{\partial x_i}\right| \quad (1)$$

Equation 1 comprises several variables and constants, including the turbulent flame speed represented by S_t, the unburned mixture density ρ_u, the local density ρ, the Favre mean value of the scalar G represented by $\tilde{G}$, the curvature κ, and the turbulent diffusivity D_t'. The first term on the right hand side of Equation 1 represents the mean turbulent burning rate, while the second term represents the impact of the flame front curvature. To solve Equation 1, it is necessary to close the system by first determining the turbulent flame speed, S_t, which is is calculated using Peters's correlation, defined as:

$$S_t = S_l + u'\left(-\frac{a_4 b_3^2}{2b_1} Da + \sqrt{\left(\frac{a_4 b_3^2}{2b_1} Da\right)^2 + a_4 b_3^2 Da}\right), \quad (2)$$

where the turbulent Damköhler number is defined as $Da = \ell\, S_l / (\ell_F\, u')$, which characterizes the ratio of flow timescales to chemical timescales; u' is the turbulence intensity (derived from the local turbulent kinetic energy), and ℓ is the integral length scale, obtained from the RANS formulation as $\ell = C_\mu^{0.75}\, k^{1.5}/\epsilon$. The laminar flame speed, S_l, is tabulated by the built-in chemistry tool. The flame thickness, ℓ_F, is estimated as $\ell_F = (\lambda_m/c_p)_0 / (\rho\, S_l)_u$, where λ_m is the molecular thermal conductivity, c_p is the specific heat, and ρ is the fluid density. Subscripts 0 and u represent in cell value, and unburned region value, respectively. Any additional constants that appear in (Equation 2) are specific to the turbulent flame speed model.

Unlike the SAGE model, which initiates combustion via an energy source that mimics the arc discharge to trigger reactions, standard ignition practice for the G-equation model is to initialize the corresponding G-field (i.e., the flame) at the spark plug electrode gap. In order to capture additional reactivities in both the unburned and burned regions, the SAGE model is coupled to the G-equation on both sides of the flame front. Due to the system's low reactivity, an uncommon practice is adopted: both an energy source and a G-field passive source are initialized in the gap vicinity. This approach increases the local reactivity and ensures successful ignition at each spark plug location, consistent with observations in the optical experiments.

Both sources are spherical with a radius of 0.5 mm, activated simultaneously at the ST. Figure 10 shows the pressure and AHRR

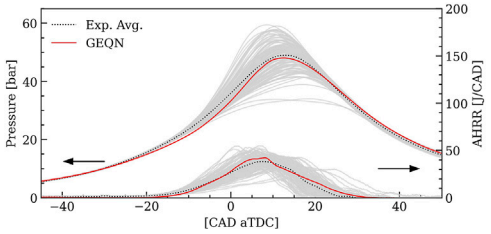

FIGURE 10
Pressure evolution for the G-equation model.

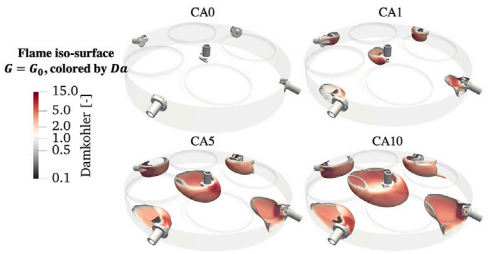

FIGURE 11
Iso-surface representing the flame ($G = G_0$), coloured by Damköhler number.

traces obtained using the G-equation combustion model, with experimental pressure traces for comparison. The combustion process is accurately captured, with small deviations observed in the numerical results, particularly at the early stages of combustion. Consequently, the model effectively characterizes the flame-flow interaction, providing a solid foundation for evaluating key aspects of the turbulence-chemistry interaction.

Figure 11 shows the visual flame development in the combustion chamber based on the iso-surface for the flame ($G = G_0$) colored by the local Da at different stages of the combustion process. At the initial stage of combustion (CA < 1), the majority of the flame front surfaces propagate with a $Da < 1$, indicating chemistry is slow and rate-determining. At this stage, the flames experience low levels of turbulence due to wall confinement, resulting in similar growth rates for all flames, as observed at CA1, where the different flame surfaces grow at a comparable rate. Once the flames surpass the spark obstacles, however, they are subjected to a wider range of turbulence level, causing Da to increase and vary in magnitude, thus affecting the flame propagation rate more significantly. At CA5, the wrinkling effect of the flame, induced by flame-turbulence interaction, accelerates flame growth, particularly for the central flame, which experiences higher turbulence and grows faster. Silva et al. (2023) reported that due to the low flame speed of NH_3, most of the combustion occurs in the corrugated flamelets regime, where the eddy length scales are larger than the flame thickness, impacting flame growth only in a kinematic manner. The increase in Da, along with the enlarged surface area of the central flame, further enhances the propagation rate. Finally, after CA10, the different flame fronts collapse and complete the consumption of the reactant charge.

Huang and Liu (2024) suggested that the inclusion of multiple sparks does not enhance turbulence levels in the chamber; instead, the advantage of this approach lies in the ignition multi-locus adjoined propagation. This behavior is akin to advanced combustion systems like the pre-chamber, where multiple ignition locations are achieved. Unlike the pre-chamber method, however, the multi-spark approach does not enhance turbulence and mixing.

6 Conclusion

In this study, a three-dimensional CFD model for SI, multi-spark NH_3 internal combustion engine was developed and validated using optical engine experiments. Because NH_3 exhibits lower reactivity compared to carbon-based fuels, it necessitates more stringent mesh resolution and spark-region modeling. Incorporating detailed spark plug geometries was found to be critical for accurately resolving early flame kernel development by improving the local flow field and temperature distribution at the onset of ignition.

When compared against natural flame luminosity measurements, the model demonstrated a high degree of qualitative agreement, indicating that key physical processes—such as ignition, flame propagation, and local turbulent mixing—are effectively reproduced. An assessment of turbulence–chemistry interactions further revealed that NH_3 combustion can shift from a chemistry-governed to a flow-governed regime, underscoring the pivotal role of turbulent kinetic energy in accelerating flame growth. Additionally, for the G-equation model (a flame-based approach), a small energy boost in the spark plug region following flame initialization was required to enhance initial kernel growth, reflecting NH_3 relatively low reactivity.

Building on this work, future investigations will leverage CFD simulations to explore advanced combustion strategies, examine varied operating parameters, and optimize engine designs.

Data availability statement

The raw data supporting the conclusions of this article will be made available by the authors, without undue reservation.

Author contributions

RM: Conceptualization, Data curation, Formal Analysis, Investigation, Methodology, Software, Visualization, Writing–original draft, Writing–review and editing. MS: Conceptualization, Formal Analysis, Investigation, Methodology, Software, Supervision, Writing–review and editing. KU: Conceptualization, Data curation, Writing–original draft, Writing–review and editing. FA: Conceptualization, Writing–review and editing. QT: Writing–review and editing. JT: Funding acquisition, Project administration, Resources, Writing–review and editing. HI: Conceptualization, Funding acquisition, Project administration, Resources, Supervision, Writing–review and editing, Formal Analysis.

Funding

The author(s) declare that financial support was received for the research, authorship, and/or publication of this article. This work was funded by the King Abdullah University of Science and Technology in Saudi Arabia.

Acknowledgments

The simulations were conducted using the high-performance computation resources of Shaheen supercomputer at KAUST Supercomputing Laboratory. The authors thank Convergent Science Inc. for providing the CONVERGE license. GPT-4 from OpenAI was used to check for English grammar and to improve writing coherence.

Conflict of interest

The authors declare that the research was conducted in the absence of any commercial or financial relationships that could be construed as a potential conflict of interest.

Publisher's note

All claims expressed in this article are solely those of the authors and do not necessarily represent those of their affiliated organizations, or those of the publisher, the editors and the reviewers. Any product that may be evaluated in this article, or claim that may be made by its manufacturer, is not guaranteed or endorsed by the publisher.

References

Amsden, A. (1997). *KIVA3V. A block-structured kiva Program for Engines with Vertical or canted valves. Tech. Rep*. Los Alamos, NM (United States): Los Alamos National Lab.LANL.

Berni, F., Cicalese, G., and Fontanesi, S. (2017). A modified thermal wall function for the estimation of gas-to-wall heat fluxes in cfd in-cylinder simulations of high performance spark-ignition engines. *Appl. Therm. Eng.* 115, 1045–1062. doi:10.1016/j.applthermaleng.2017.01.055

Bilgen, S. (2014). Structure and environmental impact of global energy consumption. *Renew. Sustain. Energy Rev.* 38, 890–902. doi:10.1016/j.rser.2014.07.004

Chiong, M.-C., Chong, C. T., Ng, J.-H., Mashruk, S., Chong, W. W. F., Samiran, N. A., et al. (2021). Advancements of combustion technologies in the ammonia-fuelled engines. *Energy Convers. Manag.* 244, 114460. doi:10.1016/j.enconman.2021.114460

De Renzis, E., Mariani, V., Bianchi, G. M., Cazzoli, G., Falfari, S., Antetomaso, C., et al. (2021). Implementation of a multi-zone numerical blow-by model and its integration with cfd simulations for estimating collateral mass and heat fluxes in optical engines. *Energies* 14, 8566. doi:10.3390/en14248566

El-Adawy, M., Nemitallah, M. A., and Abdelhafez, A. (2024). Towards sustainable hydrogen and ammonia internal combustion engines: challenges and opportunities. *Fuel* 364, 131090. doi:10.1016/j.fuel.2024.131090

EPA (2024). Fast facts on transportation greenhouse gas emissions. Available online at: https://www.epa.gov/greenvehicles/fast-facts-transportation-greenhouse-gas-emissions. Accessed: 2024-April-02

Han, Z., and Reitz, R. D. (1995). Turbulence modeling of internal combustion engines using rng κ-ε models. *Combust. Sci. Technol.* 106, 267–295. doi:10.1080/00102209508907782

Han, Z., and Reitz, R. D. (1997). A temperature wall function formulation for variable-density turbulent flows with application to engine convective heat transfer modeling. *Int. J. heat mass Transf.* 40, 613–625. doi:10.1016/0017-9310(96)00117-2

Huang, Q., and Liu, J. (2024). Preliminary assessment of the potential for rapid combustion of pure ammonia in engine cylinders using the multiple spark ignition strategy. *Int. J. Hydrogen Energy* 55, 375–385. doi:10.1016/j.ijhydene.2023.11.136

Irimescu, A., Di Iorio, S., Merola, S. S., Sementa, P., and Vaglieco, B. M. (2018). Evaluation of compression ratio and blow-by rates for spark ignition engines based on in-cylinder pressure trace analysis. *Energy Convers. Manag.* 162, 98–108. doi:10.1016/j.enconman.2018.02.014

Irimescu, A., Tornatore, C., Marchitto, L., and Merola, S. S. (2013). Compression ratio and blow-by rates estimation based on motored pressure trace analysis for an optical spark ignition engine. *Appl. Therm. Eng.* 61, 101–109. doi:10.1016/j.applthermaleng.2013.07.036

Issa, R. I., Gosman, A., and Watkins, A. (1986). The computation of compressible and incompressible recirculating flows by a non-iterative implicit scheme. *J. Comput. Phys.* 62, 66–82. doi:10.1016/0021-9991(86)90100-2

Mercier, A., Mounaïm-Rousselle, C., Brequigny, P., Bouriot, J., and Dumand, C. (2022). Improvement of si engine combustion with ammonia as fuel: Effect of ammonia dissociation prior to combustion. *Fuel Commun.* 11, 100058. doi:10.1016/j.jfueco.2022.100058

Mohan, V. R., and Haworth, D. (2015). Turbulence–chemistry interactions in a heavy-duty compression–ignition engine. *Proc. Combust. Inst.* 35, 3053–3060. doi:10.1016/j.proci.2014.06.098

Peters, N. (2001). Turbulent combustion. *Meas. Sci. Technol.* 12, 2022. doi:10.1088/0957-0233/12/11/708

Richards, K. J., Senecal, P. K., and Pomraning, E. (2021). *Converge 3.0*. Madison, WI: Convergent Science.

Silva, M., Almatrafi, F., Uddeen, K., Cenker, E., Sim, J., Younes, M., et al. (2023). Computational assessment of ammonia as a fuel for light-duty SI engines. *Tech. Rep. No. 2023-24-0013, SAE Tech Pap*. doi:10.4271/2023-24-0013

Tornatore, C., Marchitto, L., Sabia, P., and De Joannon, M. (2022). Ammonia as green fuel in internal combustion engines: state-of-the-art and future perspectives. *Front. Mech. Eng.* 8, 944201. doi:10.3389/fmech.2022.944201

Uddeen, K., Almatrafi, F., Shi, H., Tang, Q., Parnell, J., Peckham, M., et al. (2023a). Investigation into various strategies to achieve stable ammonia combustion in a spark-ignition engine. *Tech. Rep. No*. doi:10.4271/2023-24-0040

Uddeen, K., Tang, Q., Shi, H., Magnotti, G., and Turner, J. (2023b). A novel multiple spark ignition strategy to achieve pure ammonia combustion in an optical spark-ignition engine. *Fuel* 349, 128741. doi:10.1016/j.fuel.2023.128741

Uddeen, K., Tang, Q., Shi, H., Magnotti, G., and Turner, J. W. (2023c). Multiple spark ignition approach to burn ammonia in a spark-ignition engine: an optical study. *SAE Int*. doi:10.4271/2023-01-0258

Yang, R., Yan, Y., Liu, Z., and Liu, J. (2023). Formation and evolution of thermal and fuel nitrogen oxides in the turbulent combustion field of ammonia internal combustion engines. *Tech. Rep. No.* 1. doi:10.4271/2023-01-0192

Zhang, X., Moosakutty, S. P., Rajan, R. P., Younes, M., and Sarathy, S. M. (2021). Combustion chemistry of ammonia/hydrogen mixtures: jet-stirred reactor measurements and comprehensive kinetic modeling. *Combust. Flame* 234, 111653. doi:10.1016/j.combustflame.2021.111653